FATIGUE CRACK INITIATION AND PROPAGATION MODELLING USING A CYCLIC PLASTICITY CONSTITUTIVE FORMULATION

P. Čanžar, Z. Tonković, J. Kodvanj, A. Bakić, Z. Tomičević and M. Surjak
Faculty of Mechanical Engineering and Naval Architecture, University of Zagreb,
I. Lučića 5, 10000 Zagreb, Croatia

ABSTRACT

This paper presents an experimental and numerical study of the cyclic deformation and low-cycle fatigue behaviour of the aluminium alloy AlCu5BiPb–T8. The experimental program included monotonic tensile tests, symmetric and unsymmetric strain-controlled fatigue tests, ratcheting strain accumulation, fracture toughness tests, as well as fatigue crack propagation tests. Within the framework of numerical investigations an efficient algorithm for modelling of cyclic plasticity is proposed. The material model is based on multi-component forms of isotropic and kinematic hardening variables in conjunction with von Mises yield criterion. The computational algorithm is implemented into the finite element program ABAQUS and applied to the analysis of a crack growth near the notch. The accuracy of the computational procedure is tested by comparing the computed results with the real experimental data.

KEYWORDS

Low-cycle fatigue, aluminium alloy, experiment, finite element modelling, cyclic elastoplasticity, integration algorithm, crack growth

INTRODUCTION

During the service life many engineering components are subjected to cyclic loading and fatigue fracture. Experimental data and approximate numerical predictions of fatigue and fracture behaviour of metallic materials under different types of loading conditions have been presented in a large variety of literature in recent past. Therein, numerical simulation of initiation and propagation of cracks subjected to complex cyclic loading histories and estimation of fatigue life constitute a research area which is still attracting considerable interest. As presented in literature, an accurate numerical modelling of nonlinear hardening responses represents the key for describing realistic material behaviour near the crack tip [1, 2].

The purpose of this paper is to present the preliminary results of experimental and numerical investigations of ductile crack growth near the notch with the implementation of a robust cyclic plasticity theory [3-6]. The closest point projection algorithm for the integration of the cyclic plasticity constitutive model presented in [5, 6] is used to simulate low-cycle fatigue behaviour of an aluminium alloy. The integration algorithm and the corresponding consistent tangent modulus are implemented at the material point level of the available finite elements in the code ABAQUS [7] by using the user subroutine UMAT. The prediction of the crack growth is based on the material parameters generated from testing the smooth specimens. All tests are conducted at room temperature on a Walter Bai servohydraulic dynamic testing machine with a load capacity of ±50 kN. The present paper forms the continuation of work already reported in [8].

EXPERIMENTS

In the present study, a series of the uniaxial strain and stress-controlled cyclic loading experiments with several combinations of load amplitudes are performed. In this section, a short description of test procedure is given, and some selected test results are presented. The material used in the experiment is the aluminium alloy AlCu5BiPb–T8. Table 1 gives the chemical composition of the aluminium alloy. The monotonic tensile stress–strain curve with the parameters of the Ramberg-Osgood equation (n and K) are shown in Fig. 1, and the tensile mechanical properties obtained are listed in Table 2. Fig. 2 illustrates the schematic shape and geometry of specimens required for the low-cycle fatigue tests. It consists of smooth cylindrical specimens used for cyclic testing (Fig. 2a) and single edge notch bend (SENB or three-point bend) specimens (Fig. 2b) according to the standards ASTM EN 606 and ASTM E1820.

Si	Cu	Fe	Pb	Bi	Zn	Mn	Mg
0.2	5.3	0.7	0.3	0.3	0.03	0.03	0.01

Table 1: Chemical composition of the aluminium alloy AlCu5BiPb–T8 (in weight %)

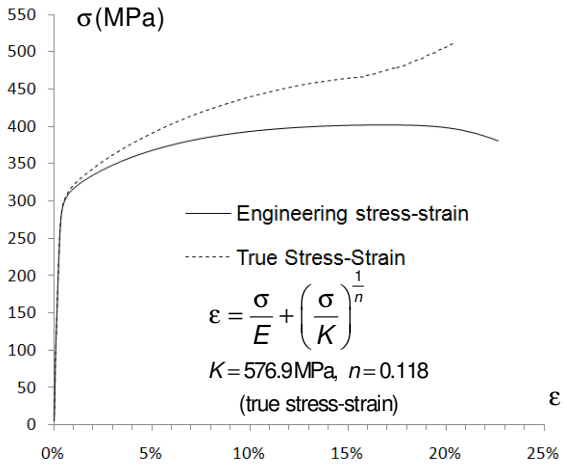

Fig. 1: Tensile stress–strain curve

Yield strength $\sigma_{0.2}$, MPa	Ultimate tensile strength σ_m, MPa	Elongation (%)	Young's modulus E, GPa	Poisson's ratio v
305	401	22	76.7	0.33

Table 2: Monotonic mechanical properties of the aluminium alloy AlCu5BiPb–T8

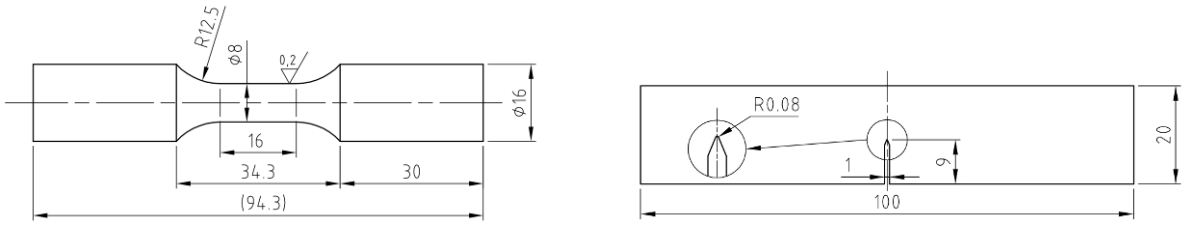

a) b)

Fig. 2: Shape and dimensions of specimens: a) cylindrical specimen for cyclic testing, b) SENB specimen for three-point bending testing

The cyclic tests are carried out under strain and stress control using an extensometer with a gauge length of 10 mm. Fig. 3 shows the stress–strain hysteresis loops of representative loading cycles obtained under fully reversed symmetric and unsymmetric strain-controlled loading. The strain amplitude ($\Delta\varepsilon/2$) in symmetric test was equal to 1.2% (Fig. 3a), while in unsymmetric test the strain amplitude and mean strain were both equal to 0.8% (Fig. 3b). Significant cyclic hardening is observed. Furthermore, comparing corresponding hysteresis loops for the symmetric and unsymmetric tests, it can be concluded that mean strain has no significant effect on the cyclic hardening behaviour of the considered material.

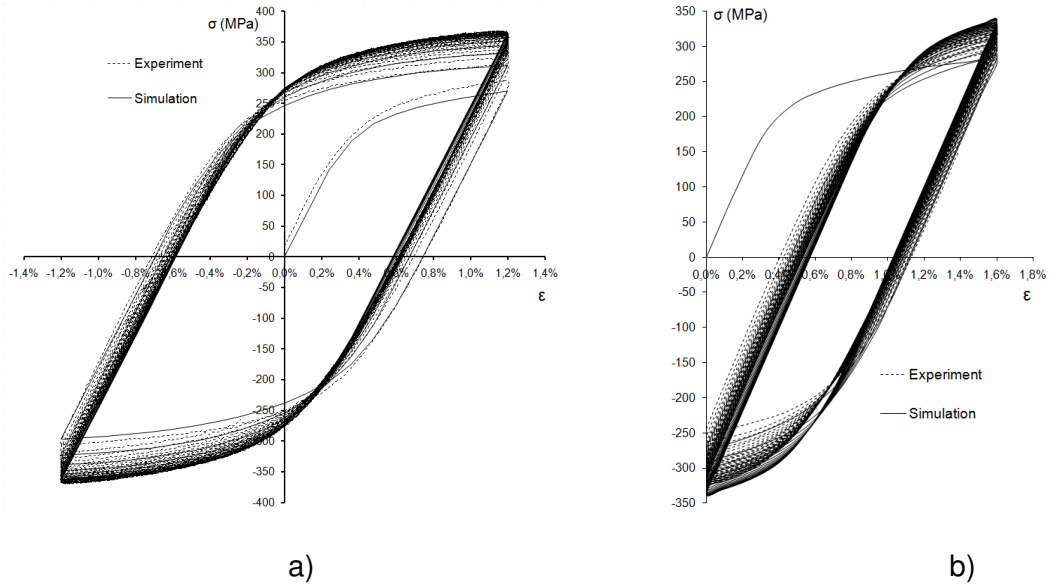

a) b)

Fig. 3: Comparison of the test data and the simulated model for representative stress–strain hysteresis loops: a) symmetric test, b) unsymmetric test

The hysteresis behaviour obtained in symmetric multiple step tests is presented in Fig. 4. Therein, the strain amplitude is increased in steps of 0.2%, while keeping the mean strain equal to zero. The number of cycles at each step was 40 and the maximum strain amplitude was equal to 1.4%. The cyclic stress-strain curve which is especially important in studies on low-cycle fatigue and crack propagation is determined by connecting the tips of the stabilized hysteresis loops obtained from specimens tested at different amplitudes. The tips of the hysteresis loops were obtained with sufficient accuracy by recording a large number of experimental points. In this investigation, the least squares technique is used to determine the material properties n' and K', which describe the Ramberg-Osgood expression for the cyclic stress-strain curve (Fig. 4).

In order to demonstrate the influence of increasing and decreasing strain amplitudes on the cyclic stress response, the variable amplitude tests [3, 4] are carried out. An example of the results obtained is given in Fig. 5. The test consists of three steps with strain amplitudes equal to 1.2%, 0.8% and 1.6%. with six cycles at each step.

All the ratcheting tests are conducted under stress control conditions with different combinations of mean stress and stress amplitude. Typical stress–strain curve of ratcheting test for the case with stress amplitude of 630 MPa and mean stress of 10 MPa is shown in Fig. 6.

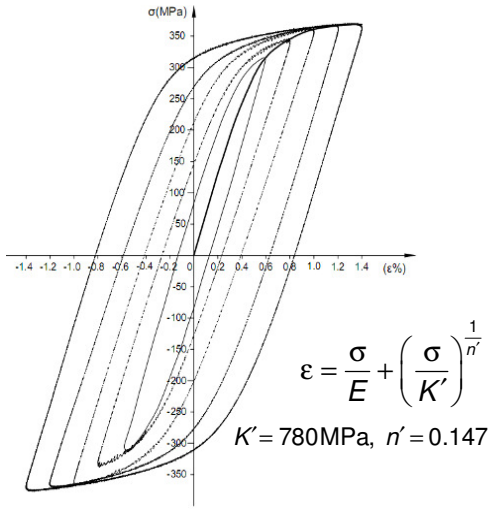

Fig. 4: Symmetric multiple step test.

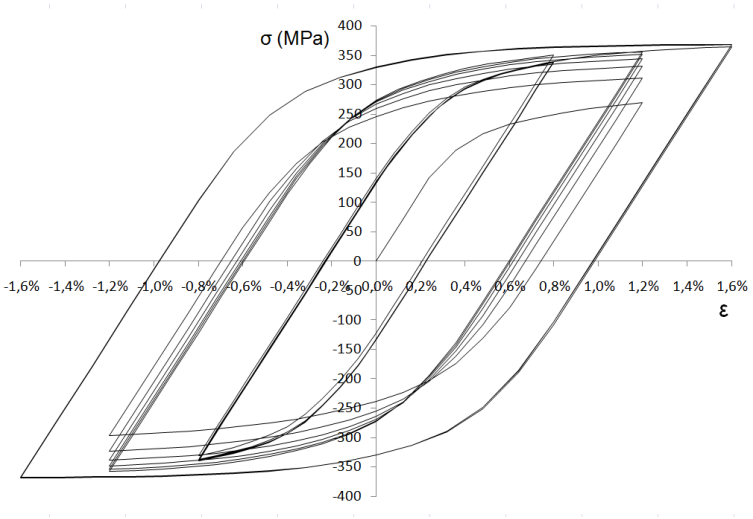

Fig. 5: Variable amplitude test with strain amplitudes equal to 1.2%, 0.8% and 1.6%

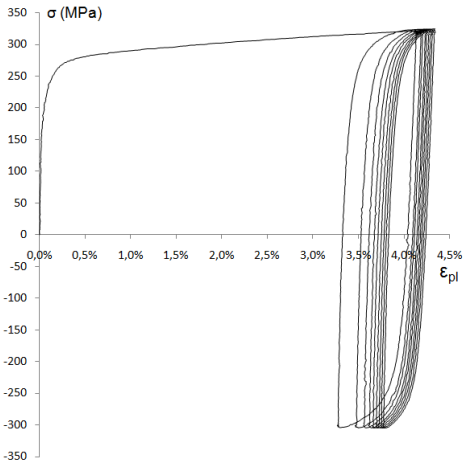

Fig. 6: Ratcheting test

Fracture toughness tests are conducted in three-point bending using SENB specimens, 10 mm thick, Fig. 2b, according to the standard ASTM E1820. For determination of the fracture toughness (K_{IC}=24 MPa $m^{1/2}$) the crack resistance curve concept is applied, where the crack increase is determined based on compliance change. Obtained diagram, load F vs. crack mouth opening displacement (CMOD), is presented in Fig. 7. For the same type of specimen geometry, fatigue crack propagation is investigated (Fig. 8). Fifteen specimens are tested under the constant amplitude loading condition with three different R-ratios of 0.1, 0.25 and 0.5. The crack length is measured using a high magnification video-camera. Figs. 9 and 10 present the crack growth results.

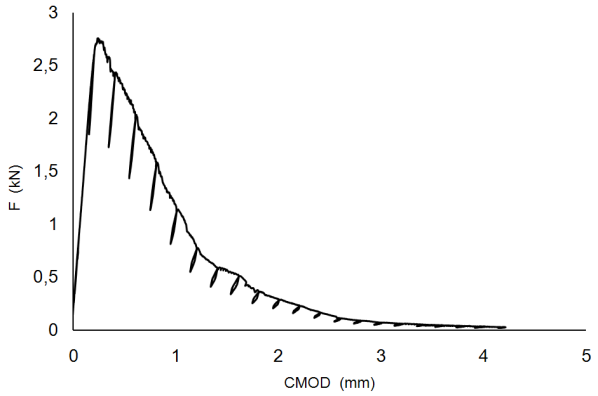

Fig. 7: Load-crack mouth opening displacement (CMOD) curve

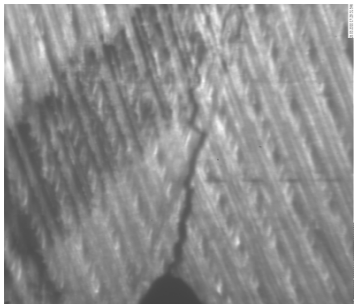

Fig. 8: Fatigue crack growth in SENB specimen

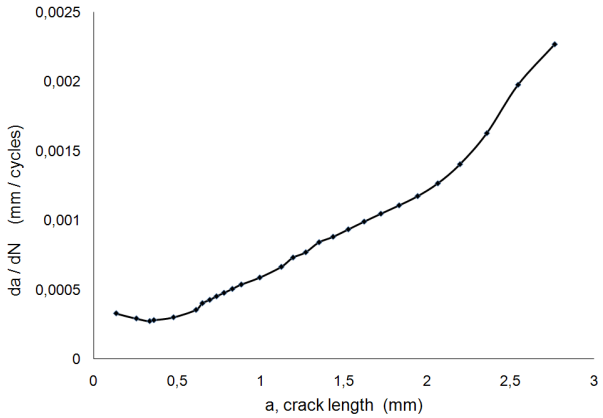

Fig. 9: Fatigue crack growth curve (R=0.1, $\Delta F/2$=1.08 kN)

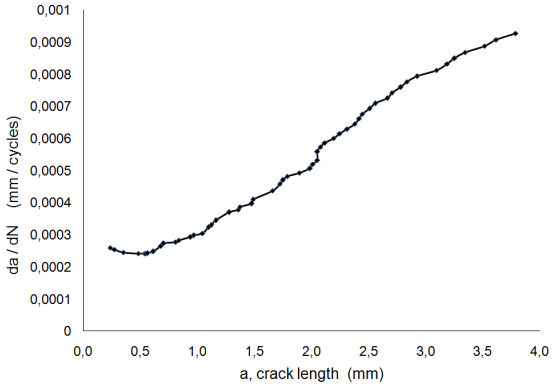

Fig. 10: Fatigue crack growth curve (R=0.25, $\Delta F/2$=0.9 kN)

NUMERICAL FORMULATION

The applied constitutive model includes highly nonlinear multi-component forms of kinematic and isotropic hardening functions in conjunction with von Mises yield criterion. Under the assumptions of small strain and associativity of the flow rule, an isothermal material behaviour is considered. The basic constitutive equations of the material model are compiled in Table 3. Herein the Latin indices take the values 1, 2 and 3. S^{ij} and α'^{ij} are the deviatoric components of the stress tensor σ^{ij} and back stress tensor α^{ij}, respectively. λ is the plastic multiplier while C^{ijkl} abbreviates the constitutive tensor describing the material response. The material parameters are calibrated using test data from a constant amplitude tests (Fig. 3) and multiple step tests (Fig. 4). The following values are adopted: $A_1 = 16.54$ GPa, $A_2 = 112.602$ GPa, $B_1 = 271.6$, $B_2 = 2149.8$, $C_1 = 18.15$, $C_2 = 0$, $D_1 = 105$ MPa, $D_2 = 0$.

Decomposition of total strain rate into elastic and plastic parts:	$\dot{\varepsilon}_{ij} = \dot{\varepsilon}^{\,e}_{ij} + \dot{\varepsilon}^{\,p}_{ij}$.	(1)
Stress tensor rate:	$\dot{\sigma}^{ij} = C^{ijkl}\,\dot{\varepsilon}_{kl}$.	(2)
The von Mises-type yield condition:	$F = \frac{1}{2}\left(S^{ij} - \alpha'^{ij}\right)\left(S_{ij} - \alpha'_{ij}\right) - \frac{1}{3}k^2(a) \le 0$.	(3)
Associative flow rule:	$\dot{\varepsilon}^{\,p}_{ij} = \dot{\lambda}\frac{\partial F\left(\sigma^{ij}, \alpha^{ij}, a\right)}{\partial \sigma^{ij}}$.	(4)
Nonlinear kinematic hardening rule:	$\alpha^{ij} = \sum_{m=1}^{2} \alpha^{ij}_{m}$, where $\dot{\alpha}^{ij}_{m} = A_m\,\dot{\lambda}\,\eta^{ij} - B_m\,\dot{\varepsilon}^{p}_{eqv}\,\alpha^{ij}_{m}$, $\dot{\varepsilon}^{p}_{eqv} = \sqrt{\frac{2}{3}\dot{\varepsilon}^{p}_{ij}\,\dot{\varepsilon}^{p\,ij}}$.	(5)
Nonlinear isotropic hardening rule:	$k = \sigma_Y + a$.	(6)
Internal variable describing isotropic hardening:	$a = \sum_{m=1}^{2} a_m$, where $\dot{a}_m = C_m\left(D_m - a_m\right)\dot{\varepsilon}^{p}_{eqv}$.	(7)
Consistency condition in Kuhn-Tucker form:	$F\left(\sigma^{ij}, \alpha^{ij}, a\right) \le 0, \quad \dot{\lambda} \ge 0, \quad \dot{\lambda}\,F\left(\sigma^{ij}, \alpha^{ij}, a\right) = 0$.	(8)
Relative stress tensor:	$\eta^{ij} = \sigma^{ij} - \alpha^{ij}$.	(9)

Table 3: Basic constitutive equations

To integrate the elastoplastic constitutive model a computational strategy based on the closest point projection scheme is applied where the rates of all measures are replaced by their incremental values. The proposed integration method yields only one scalar nonlinear equation which has to be solved for the plastic multiplier λ using the Newton iteration procedure. After determination of the plastic multiplier, the updated values of stresses as well as all internal variables can be calculated. In order to preserve numerical efficiency of the global iteration strategies, the consistent elastoplastic tangent modulus, derived by linearization of the updated algorithm, is applied. A step by step formulation is summarized in Table 4. More details concerning the applied computational strategy can be found in References [5, 6]. The derived computational algorithm is implemented in the software ABAQUS/Standard by using the user-defined material (UMAT) subroutine [7].

---

1. Compute elastic trial state at time ${}^{n}t$:
$$ {}^{n}\sigma^{ij}_{\text{trial}} = {}^{n-1}\sigma^{ij} + {}^{n-1}C^{ijkl}\ {}^{n}\Delta\varepsilon_{kl} . $$
2. Check for yielding:
$$ {}^{n}F_{\text{trial}} = J_2\left({}^{n}\sigma^{ij}_{\text{trial}}\right) - \frac{1}{3}k^2\left({}^{n-1}a\right) > 0 , $$
no $\rightarrow$ ${}^{n}\lambda = 0$ $\rightarrow$ elastic step $\rightarrow$ go to (5),
yes $\rightarrow$ ${}^{n}\lambda > 0$ $\rightarrow$ plastic step.
3. Plastic corrector phase:
$$ {}^{n}\eta^{ij} = {}^{n}\sigma^{ij} - {}^{n}\alpha^{ij} = {}^{n}A^{ij}_{kl}\ {}^{n}\eta^{kl}_{\text{trial}} , $$
where $ {}^{n}\sigma^{ij} = {}^{n}\sigma^{ij}_{\text{trial}} - {}^{n-1}C^{ijkl}\ {}^{n}\Delta\varepsilon^{\text{p}}_{kl} $, $ {}^{n}\alpha^{ij} = \sum_{\text{m}=1}^{2}\left({}^{n}U_{\text{m}}\ {}^{i-1}\alpha^{ij}_{\text{m}} + 2\,{}^{i}U_{\text{m}}\ {}^{i}\lambda\ A_{\text{m}}\ {}^{i}\eta^{ij}\right) $,
$$ {}^{n}U_{\text{m}} = \frac{1}{1+2A_{\text{m}}\ {}^{n}\lambda\ {}^{n}k} , \qquad {}^{n}\eta^{ij}_{\text{trial}} = {}^{n}\sigma^{ij}_{\text{trial}} - \sum_{\text{m}=1}^{2}{}^{n}U_{\text{m}}\ {}^{n-1}\alpha^{ij}_{\text{m}} , $$
$$ {}^{n}A^{ij}_{kl} = \frac{1}{1+2\,{}^{n}\lambda\left(\sum_{\text{m}=1}^{2}{}^{n}U_{\text{m}}\ B_{\text{m}} + G\right)}\left[\delta^{i}_{k}\delta^{j}_{l} + \frac{2\,{}^{n}\lambda G\left(1-2\nu\right)}{2\,{}^{n}\lambda G\left(1+\nu\right)+3\left(1-\nu\right)\left(1+2\sum_{\text{m}=1}^{2}{}^{n}\lambda\,{}^{n}U_{\text{m}}\,B_{\text{m}}\right)}\ a_{kl}\,a^{ij}\right] . $$
Yield condition (nonlinear scalar equation):
$$ {}^{n}F = {}^{n}J_2\left({}^{n}U_{\text{m}}, {}^{n}\lambda, {}^{n}\eta^{ij}_{\text{trial}}\right) - \frac{1}{3}k^2\left({}^{n}a\right) = 0 \rightarrow \text{solution for } {}^{n}\lambda . $$
4. Compute consistent elastoplastic tangent modulus.
5. Update all internal variables and compute stress and back stress at time ${}^{n}t$.

Table 4: Integration algorithm

COMPARISON OF EXPERIMENTAL AND NUMERICAL RESULTS

Fig. 3a shows a comparison of the numerical predictions and the test data obtained from the symmetric strain-controlled cyclic experiment. Good agreement of the solutions is exhibited except for the first cycle, since the kinematic hardening component is calibrated using the stabilized stress-strain curve. Additionally, the accuracy of the computational procedure is tested by comparing the computed stress-strain hysteresis loops with experimental data for unsymmetric test, Fig. 3b. As evident from figure, the stress-strain response obtained from the numerical simulations is in a good agreement with the physical behaviour of the material. It should be noted here that the material parameters used in all numerical simulations are identical to those used in symmetric strain-controlled cyclic test. The model is afterwards utilized to study the crack tip cyclic deformation and to predict

crack growth in a SENB type specimen. The geometry of SENB specimens is meshed into four-node first order plane-strain elements. Refined mesh is created near the crack tip which is modelled as initially blunted. During the fatigue simulation, the damage accumulation is monitored at the notch and the crack tip. The crack growth experimental results are presented using the relationship between the crack length measured from the root of the notch and the crack growth rate, as shown in Figs. 9 and 10. The numerical results for the crack growth are not reported in this paper. These results represent the content of the current research.

CONCLUSION

The cyclic deformation and low-cycle fatigue behaviour of the aluminium alloy AlCu5BiPb–T8 has been studied experimentally and numerically. Material properties investigated through the experimental program are monotonic and cyclic stress-strain curves, fracture toughness and fatigue-crack propagation in the aluminium alloy. A numerical algorithm for modelling of cyclic plasticity, employing a rather realistic constitutive model with highly nonlinear isotropic and kinematic hardening responses is proposed. The material model employs the nonlinear hardening rules derived by superimposing of several hardening laws of the same type, which are based on the Armstrong-Frederick equations. The accuracy of the computational procedure is tested by comparing the computed stress-strain hysteresis loops with experimental data.

REFERENCES

[1] Ding, F.; Feng, M.; Jiang, Y.:
Modeling of fatigue crack growth from a notch
Int. Journal of Plasticity, 23 (2007), pp. 1167–1188

[2] Fan, F.; Kalnaus, S.; Jiang, Y:
Modeling of fatigue crack growth of stainless steel 304L
Mechanics of Materials, 40 (2008) No. 11, pp. 961-973

[3] Hopperstad, O.S.; Langseth, M; Remseth, S:
Cyclic Stress-Strain Behaviour of Alloy AA6060, Part I
Int. Journal of Plasticity, 11 (1995) No. 6, pp. 725-739

[4] Nukala, K.P.V.V.:
A return mapping algorithm for cyclic viscoplastic constitutive models
Comput. Meth. Appl. Mech. Eng., 195 (2006), pp. 148-178

[5] Sorić, J.; Tonković, Z.; Krätzig, W.B.:
A new formulation of numerical algorithms for modeling of elastoplastic cyclic response of shell-like structures
Computers & Structures, 78 (2000), pp. 161-168

[6] Tonković, Z.; Sorić, J.; Skozrit, I.:
On Numerical Modeling of Cyclic Elastoplastic Response of Shell Structures
Computer Modeling in Engineering & Sciences (CMES), 26 (2008) No. 2, pp. 75-90

[7] Hibbitt, Karlsson & Serensen, Inc.:
ABAQUS/Standard. User's guide and theoretical manual, Version 6.9, (2009)

[8] Čanžar, P.; Tonković, Z.; Kodvanj, J.; Bakić, A.; Tomičević, Z.:
Modelling of cyclic plasticity and crack propagation
International Conference on Fracture and Damage Mechanics, Nagasaki, Japan (2010)

Corresponding author: predrag.canzar@fsb.hr